LANGMUIR

pubs.acs.org/Langmuir Article

Soft Contact Mechanics with Gradient-Stiffness Surfaces

Md Mahmudul Hasan, Christopher L. Johnson, and Alison C. Dunn*



Cite This: https://doi.org/10.1021/acs.langmuir.2c00296



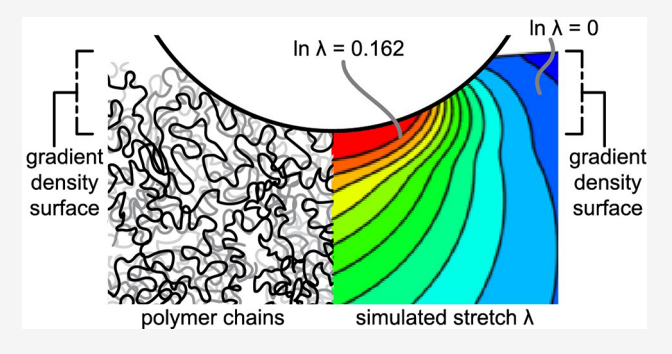
ACCESS I

Metrics & More

Article Recommendations

Supporting Information

ABSTRACT: The stiffness in the top surface of many biological entities like cornea or articular cartilage, as well as chemically cross-linked synthetic hydrogels, can be significantly lower or more compliant than the bulk. When such a heterogeneous surface comes into contact, the contacting load is distributed differently from typical contact models. The mechanical response under indentation loading of a surface with a gradient of stiffness is a complex, integrated response that necessarily includes the heterogeneity. In this work, we identify empirical contact models between a rigid indenter and gradient elastic surfaces by numerically simulating quasi-static indentation. Three key case studies revealed the specific ways in which (I) continuous gradients, (II) laminate-layer



gradients, and (III) alternating gradients generate new contact mechanics at the shallow-depth limit. Validation of the simulation-generated models was done by micro- and nanoindentation experiments on polyacrylamide samples synthesized to have a softer gradient surface layer. The field of stress and stretch in the subsurface as visualized from the simulations also reveals that the gradient layers become confined, which pushes the stretch fields closer to the surface and radially outward. Thus, contact areas are larger than expected, and average contact pressures are lower than predicted by the Hertz model. The overall findings of this work are new contact models and the mechanisms by which they change. These models allow a more accurate interpretation of the plethora of indentation data on surface gradient soft matter (biological and synthetic) as well as a better prediction of the force response to gradient soft surfaces. This work provides examples of how gradient hydrogel surfaces control the subsurface stress distribution and loading response.

1. INTRODUCTION

The mechanics of soft systems with changing, or gradient, properties near the surface are of interest in both biological and synthetic systems. In biological systems, local properties provide critical information about the health and function of cells and tissues. However, cells and tissues often exhibit a layered, or laminate, structure.2 This structure can facilitate a variety of functions including mass transport,³⁻⁵ thermal insulation,⁶ and managing mechanical stress.^{7,8} One system of particular interest is that of the eye: the tough sclera maintains the intraocular pressure, but that mechanically strong tissue is topped with the more compliant layer of stratified epithelial cells, which is again topped by flexible microvilli and glycocalyx, finally manifesting in the viscous, aqueous gel of the tear film (Figure 1A). From a mechanical perspective, the monotonic increase in compliance through these layers can be considered a gradient of stiffness decreasing toward the outer surface. In synthetic systems, work has identified a property of hydrogel surfaces that is remarkably similar to laminate biological tissues: a very compliant layer atop a stiffer one. While contact lens companies have started using this to design more comfortable products, 10,11 there is evidence that softer layers also inherently appear: early hydrogel work showed a difference in hydrogel composition near mold surfaces, 12,13

implicating the physics of the polymerization process.¹⁴ Probebased techniques used to assess properties of polyacrylamide hydrogels revealed a less-dense surface layer which controls the shallow-depth indentation properties as measured by AFM. 15 Work by Sudre et al. 16 predicted that all acrylamide hydrogels synthesized by simultaneous chain extension and cross-linking would exhibit a less-dense surface layer unless specific actions were taken to suppress it. For polyacrylamide molded against polystyrene, the "brushy" layer is estimated to be on the order of 20 μ m in thickness. ¹⁷ While it would be ideal if this soft surface layer were homogeneous, providing a clear laminate structure, that is unlikely due to its formation at the interface between the prepolymer solution and a mold. The process of chemical cross-linking could involve effects from the surface energy of the mold material, adsorbed species on the mold, and the depletion of available polymer and cross-linker as the synthesis comes to completion. 18 Thus, this soft surface layer also has a gradient of density from the bulk out to the most superficial polymer chains extending into an aqueous bath (Figure 1B).

Received: February 5, 2022 Revised: July 13, 2022



Figure 1. Similar gradient layers in human corneal tissue and a hydrogel surface. (A) Histological section of central cornea (\times 17500) showing a layer of mucus $\sim 1~\mu m$ thick at the outside of the corneal epithelium. The corneal gradient extends from the tough sclera through the epithelium to the microvilli and mucus layer. Reproduced with permission from ref 9. Copyright 1985 Association for Research in Vision and Ophthalmology. (B) A gradient in density of a hydrogel surface as it swells into an aqueous bath, shown as a polymer mesh network schematic.

Probe-based techniques on sample surfaces provide one of the most suitable approaches for assessing the mechanical response of gradient-property surfaces; this is because the depth of interrogation is controlled. However, the confounding problem of interpreting the force-depth data is that the integrated force response at a particular depth necessarily includes the mechanics of the surface to that depth and below. In response, researchers have taken a variety of approaches, starting with the most simple of fitting data to classical and established contact models: Hertz, JKR, and others. 19-23 Others have moved beyond homogeneous models to acknowledge a single softer layer atop a stiffer one, 11,24,25 with associated elastic foundation models. Whether a half-space or a single laminate surface, both of these models assume homogeneity and linear elasticity. For many biological samples, their inherent heterogeneity is the biggest limit to appropriately interpreting the forces and displacements measured by using these probe-based techniques. While homogeneity of some pseudo-isotropic tissues can be assumed at the micro- or nanoscale, most materials of interest have heterogeneity that exists down to the smallest scales. For example, tissues are composed of cells and their extracellular matrix—cells are lipid membranes encapsulating fluids, and the extracellular matrix is deposited and grown from the molecular scale. Thus, contact models that allow for depth-dependent properties may significantly increase the ability to diagnose medical conditions which disproportionately affect a particular tissue layer. Similarly, the softer surface skin layers on hydrogels have been shown to control their lubricating ability, 26,27 so the characterization and exploitation of these layers will be necessary for design of soft surfaces that interface with delicate biological tissues.

Further theoretical and experimental advances have been made toward the indentation response of soft and hydrated materials. First, work has focused on more accurate constitutive models, specifically considering hyperelasticity, 28 hyperelasticity with adhesion,²⁹ viscoelasticity, and poroelasticity applied to systems that are expected to exhibit those properties. Combined viscoelasticity and poroelasticity models have been applied with success;³⁰ however, complications arise when considering possible interdependencies of these properties, and most necessarily assume isotropy of the sample. Another approach is to treat the sample as continuous but orthotropic, 31 which can describe fiber-reinforced materials. Properties of very compliant or biologically derived samples can be fit with these models given the volume being probed is sufficiently small to be described by a particular, homogeneous constitutive response. Second, work has recast a continuous

gradient into a variety of discrete lamina, with progressive model fitting to ascertain stiffnesses at various stages of the indentation. 32,33 The most thorough mechanics treatment of gradient, or graded, surfaces is from the functionally graded materials (FGM) community, appearing most relevantly in Giannakopoulos and Suresh³⁴ as well as Perriot and Barthel.³⁵ In these works a gradient of stiffness E is assigned to a halfspace through a simple power law changing with depth z: E = $E_0 z^k$, and the resulting stress and deformation fields are derived. Importantly, the force-depth relation deviated from the Hertz contact case $(F \propto d^{3/2})$ with a power associated with the extent of stiffness change, k, initially assigned to the halfspace: $(F \propto d^{3+k/2})$. A variety of analytical elasticity solutions exist, 36-40 and may be helpful, but they have limited applicability to solve for local gradient properties of complex biological and soft samples because of the advanced approaches and solution methods required. Zelentsov et al. 41 attempted to bridge this by providing simplified solutions, but they still require simplification of a gradient surface into pseudo-homogeneous regions. The authors believe that the complexity of the theoretical approaches or the reliance on elasticity in the small-strain limit has prevented adoption to the indentation data taken on biological and soft materials. Thus, on the basis of the current state of the field, there is a need to provide translatable definitions and guidance to inform interpretation of extensive indentation data being generated from both biological and soft materials for potentially transformative advancements in health science.

In this work, we hypothesize that gradient soft surface layers have contact models whose power relationships between force and indentation depth are determined by the functional form of the gradient and the thickness of the gradient layer with respect to the size of the indenting probe. To prove this hypothesis, we identify three case studies with specific gradient-stiffness surfaces to discover the particular effects of the following: (A) the functional form of the stiffness, i.e., the rate of change of stiffness with depth; (B) the extent of the gradient with respect to probe size; and (C) how accurately laminate composites approximate a continuous linear gradient. We find that the outer layer affects the entirety of the forcedepth curves. The stiffness of the bulk beneath the softer surface layer can be extracted from the data of latter segments by using the Hertz contact model; however, it fails to fit at shallow depths, and surface properties are overlooked. By use of a derivative method, the gradients in stiffness at the surface are revealed, and the deviation from expected models provides a quantitative connection between the stiffness gradient and

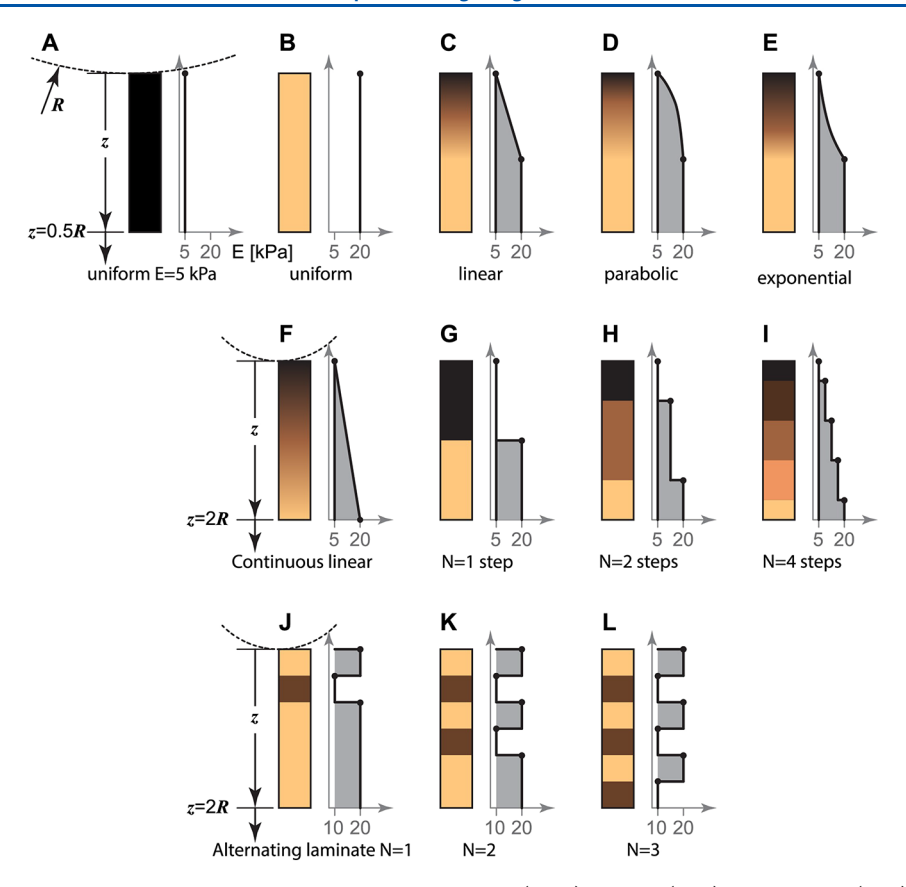


Figure 2. Schematics showing the change of modulus with depth for in case I (A–E), case II (F–I), and case III (J–L). Stiffness gradients are indicated by a color scale from light to dark corresponding to a reduction of stiffness. All gradients are shown in (C–E) for the case of extending into the sample to a depth of 0.27R. Samples of uniform modulus of E = 5 and E = 20 kPa are shown in (A) and (B), respectively. From (C) to (E), three functional forms, such as linear, parabolic, and exponential gradient, are shown using both the color scale and a line plot for continuous gradient layer (case I). From (G–I), schematics show the change of modulus with depth for samples in laminate gradient layers (case II). From (J–L), schematics show the change of modulus with depth for samples in alternating laminate layers (case III).

the integrated force response. For linearly graded layers, simulated results allow a direct translation between the contact-observed stiffness response and the input material stiffness profile. We then compare the simulated data with instrumented indentation of polyacrylamide surfaces with spherical probes both at the microscale and at the nanoscale. Finally, the experimental polyacrylamide indentations are assessed by using the translation schema to determine an approximate material stiffness profile of the experimental hydrogel gradient layer. We conclude that simulation tools can provide clear trends of the integrated contact response of such gradient surface. In addition, it helps to interpret and to predict the real contact responses of both synthetic and biological materials that likely have gradient soft surfaces.

2. MATERIALS AND METHODS

2.1. Cases Studied. *2.1.1. Nomenclature and Reference Case.* The contact mechanics for soft materials have two controlling dimensions: the radius of the indenter and the thickness of the sample being indented. The ratio of these determines the regime, that is, whether the sample can be treated as an infinite half-space with no far-field effects or the sample may have substrate effects. ^{42,43} For all simulations in this work, the dimensions are all reported with respect to the radius of the indenter, *R.* The total sample thickness in all cases is 10*R.*

These controlling dimensions along the vertical direction interact with the elasticity of the sample through the modulus of elasticity, or Young's modulus, *E*. Two anchoring moduli of elasticity were chosen

to bound these simulations: the highest modulus which typically represents a bulk property is defined as $E_{\rm b}=20\,$ kPa; the lowest modulus which typically represents a more compliant surface property is defined as $E_{\rm s}$, which is 5 kPa for all considered cases except case III. The Poisson ratio, ν , is considered as 0.499 for all cases. The cases are described as follows:

2.1.2. Case I: Continuous Gradient Layer. If a gradient layer exists at the surface of hydrogels due to molding, swelling, or grafting, it has some elasticity distribution into the depth. Here, two parameters are taken into consideration as case I: thickness of the gradient layer, d_b and the functional form of the elasticity distribution in the gradient layer. The depth of the gradient layer is investigated over a range of 1–20% of the slab thickness with a logarithmic increment (i.e., the gradient layer extends to 1, 2.7, 7.4, and 20% of the total sample thickness, 10R). Thus, the four gradient layer thicknesses are $d_l = 0.1R$, 0.27R, 0.74R, and 2R. At each d_b three different functional forms of the distribution are considered: linear, exponential, and parabolic (see Figure 2C–E). In total, a matrix of 12 conditions (four depths and three forms) are found. For all cases, the modulus at the extreme surface and the modulus of the bulk layer are kept constant as $E_s = 5$ kPa (Figure 2A) and $E_b = 20$ kPa (Figure 2B), respectively.

2.1.3. Case II: Laminate Gradient Layers. A layering of biological tissue 33,44 or synthesis of a laminate material also provides a compelling case study of layers of discrete stiffness rather than a continuous gradient as in case I. The ability of discrete layers to approximate the integrated contact response of a continuous gradient layer is assessed here as case II. To do this, the continuous gradient layer with a depth of $d_l = 2R$ is replaced with a number of laminated layers with modulus varied from $E_{\rm s} = 5$ kPa to $E_{\rm b} = 20$ kPa. The moduli of laminated layers are chosen in such a way that the depth-

average elasticities for different laminated layers are approximately equal to the continuous linear gradient sample with same d_l . The number of layers is varied as N=1, 2, 4, and 8, and $E_{\rm b}=20$ kPa is considered for all cases. The schematic shown in Figure 2G–I represents the comparative thickness and the modulus of each layer. The thickness of each layer in the overall gradient layer decreases as $d_l=R$, 0.67R, 0.4R, and 0.22R as the number of layers increases as N=1, 2, 4, and 8, respectively. For case II, the control sample is defined as continuous linear gradient with a depth of $d_l=2$ R, as shown in Figure

2.1.4. Case III: Alternating Laminate Layers. Materials of structured compliance, such as alternating stiff—soft composites for directing biological responses, 45,46 are the final case of interest. Alternating laminate stiffness is also found in biological tissues, for example, in the cellular architecture of breast cancer. Thus, as case III, we consider a composite layer structure of two alternating laminates with different and constant moduli to investigate the overall mechanical response. We consider three cases of N=1, 2, and 3, where N is the number of bilayers above the bulk layer having $E_{\rm b}=20$ kPa, which is identical with the prior cases. As shown in Figure 2J–L, each bilayer contains a top stiffer layer followed by a softer bottom layer with modulus of 20 and 10 kPa, respectively. The thickness of each bilayer is constant as 0.67R.

2.2. Simulation Methods. An axisymmetric model of conventional spherical indentation was created by using finite elements (ABAQUS 6.14 software, 3DS, France). The horizontal and vertical directions were chosen as the r-axis and z-axis, respectively, as shown in Figure 3. A rigid spherical indenter of radius $R \equiv 5$ (SI base unit)

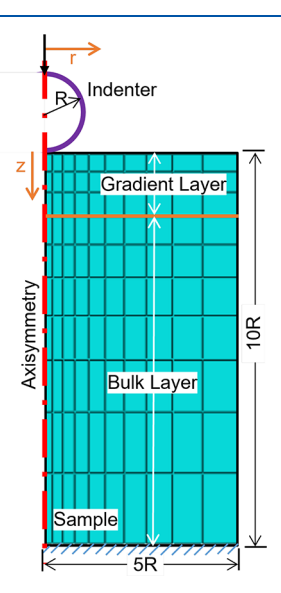


Figure 3. Schematic of the simulation setup with all necessary dimensions and boundary conditions. The indenter radius R and the sample dimensions are drawn to scale. The 2D rectangular sample section had dimensions of $r \times z = 5R \times 10R$, consisting of the gradient layer and the bulk layer. The comparative thickness of each layer varied for each of the three cases. A refined mesh in the vicinity of the contact was used. Here, 11×11 nodes are shown in the schematic to represent the 101×101 nodes in the actual setup.

was translated progressively in the positive z-direction (vertically downward) into a rectangular sample. Keeping the total number of node constant, we have simulated samples with different widths and found an optimum sample dimension as $r \times z = 5R \times 10R$, which has higher sensitivity near contact and minimum lateral edge effect in force response. As ABAQUS has no constitutive system for units, we can interpret the results at different length scales, assuming there is no length-scale effect. As such, we kept all dimensions in terms of R. We assumed frictionless elastic contact for the simulation setup. The following boundary conditions were applied: the bottom of the

sample was fixed, the left z-axis of the sample was chosen as the axis of symmetry (and prohibited from any rotation and lateral movement), and the indenter was constrained to vertical movement only. The nodes of right vertical plane are defined as traction free boundary condition. 48,49

To introduce varying elasticity within the gradient layer of each sample, we used an arbitrary pseudo-temperature as a proxy for stiffness. A similar method has been used previously to model a functionally graded material (FGM) with spatially varied properties. 50,51 Here, we assigned different arbitrary temperatures to node sets corresponding to layers at specific depths. Then, a discrete stiffness value was assigned to each arbitrary temperature. Thus, the simulation setup considered the sample to have varying elasticity with depth. To improve sensitivity, a fine mesh was chosen, with further mesh refinement near the vicinity of the contact (Figure 3). There were 101 × 101 total nodes in the sample. The sample was modeled by using ABAQUS' CAX4RH elements, with 10000 total elements.⁵² The minimum node spacing (distance between two adjacent nodes) was 0.0078R and 0.0157R in the r- and z-directions, respectively. The increment of progressive indentation depth, d, was automatically chosen by the solver such that the size of the subsequent z-increment adjusted based on how quickly the solution converged. The reaction force F from the sample due to the vertical displacement of the indenter, d, was recorded and plotted as the F-d curve.

2.3. Experimental Methods and Materials. 2.3.1. Hydrogel Synthesis. Polyacryalmide hydrogels were synthesized from a solution of acrylamide (Aam) monomer, methylenebis(acrylamide) (BisAam) cross-linker, tetramethylethylenediamine (TEMED), and ammonium persulfate (APS). These solutions were combined to create a prepolymer solution of 7.5% Aam (all on a weight-per-weight basis), 0.3% BisAam, 0.15% TEMED, and 0.15% APS. This solution was quickly poured into full-contact polystyrene or glass molds: AFM experiments used samples with diameter 15 mm and thickness 2 mm (Figure S1B), while microscale experiments used hydrogel slabs of diameter 25 mm and height 5 mm (Figure S1A). After the samples were allowed to cure in the mold for 30 min, they were placed in a bath of deionized water for at least 24 h prior to testing. All testing was done in a submerged configuration.

2.3.2. Microscale Tribometer Indentation. Short-duration displacement-controlled indentation was performed by using a custom tribometer described in previous work by Dunn et al. ¹¹ This tribometer uses a box cantilever flexure with normal stiffness of 49.14 μ N/ μ m and a steel probe of radius 2 mm (Figure S1A). Indentation was conducted at a constant loading rate of 25 μ m/s (Table S1), reaching a peak load of 1000 μ N; the dwell time was zero. Signals representing the normal force and stage displacement were acquired at a rate of 100 Hz. Experiments were performed on areas of the gel at least 4 mm away from each other, with 10 min in between each indentation to ensure no history-dependent results.

2.3.3. AFM Nanoindentation. Cantilever Calibration. Colloidalprobe nanoindentation was performed on molded hydrogel samples to investigate the surface mechanical properties by using a Cypher AFM (Asylum Research, Santa Barbara, CA). A borosilicate glass colloidal probe with a diameter of 10 μ m (confirmed via optical microscope) was used for the indentation experiments (model:CP-qp-CONT-BSG-B, NanoAndMore, Watsonville, CA). A well-established noncontact two-step calibration method⁵³ was used to estimate the normal spring constant k and the InvOLS (inverse optical lever sensitivity, units: nm/V) in liquid. As a first step, the spring constant kin air was measured by using the GetReal routine (this routine uses both the thermal noise and Sader methods⁵⁴), a proprietary software feature to the Cypher AFM. We also calculated k using an alternative method called the Sader GCI method 55 and found similar values. As kis a geometric and material property, it does not change when the experimental medium is changed from air to water. Thus, as a second step, InvOLS in liquid was estimated by using the thermal Sader method while keeping k constant, equal to the value calculated for air.

Nanoindentation. The polymerized, swollen hydrogel sample was kept at room temperature for an hour before the indentation to avoid any temperature effects during the experiment. The sample was attached to the AFM sample holder by using underwater epoxy adhesive (Mr. Stick's, Fair Oaks, CA), and during the experiment, the AFM tip and the sample were submerged in water. During tip calibration, the tip was kept far away from the sample to avoid any surface interaction between them. Then, during the indentation, the indent speed was kept constant as 2 μ m/s as used in similar experiments by Shoaib et al. ⁵⁶ For each sample, indentation was performed on at least 10 different spots at least 50 μ m apart. All 10 measurements were used to estimate the mean and standard deviation of the modulus of elasticity as fit to the measured data as described in section 2.4.

2.4. Indentation Analysis Method. Traditionally, indentation analysis involves curve fitting of a contact model to determine both the reduced modulus and the initial point of contact. For example, in the Hertzian contact model (eq 1), the force response is dependent on the probe geometry and the reduced modulus E^* as well as the probe indentation depth $d.^{57}$ As shown in Figure 4A, our simulated

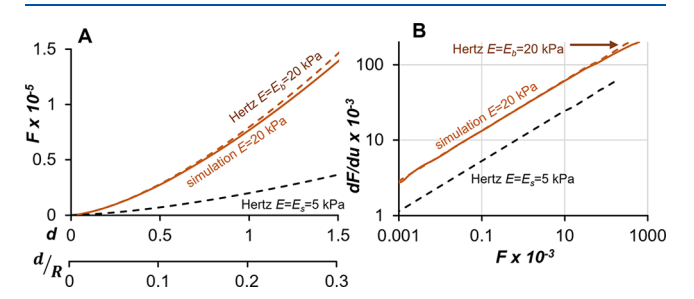


Figure 4. (A) Plot showing force vs indention depth for two reference Hertz contacts using a modulus of $E=E_{\rm b}=20~{\rm kPa}$ and $E=E_{\rm s}=5~{\rm kPa}$. For validation, the simulation result for a sample with constant modulus of $E=20~{\rm kPa}$ is also shown. A second x-axis is added in (A) as a reference to the depth d/R associated with each force value F to show the maximum allowable depth according to a typical Hertzian model application. (B) Data plotted on a log–log scale using the Garcia method (eq 2). Units are SI base units.

force response for homogeneous sample closely agrees with Hertz model (difference is less than 5%) up to d < 0.3R. Other researchers from different groups also reported d < 0.3R as a safe limit for predicting Hertz behavior in soft materials. ^{29,43,58,59} In addition, we have performed simulation with hyperelastic materials of Mooney–Rivlin (MR) type, and for d < 0.3R, the force response of MR sample is overlapped with the homogeneous sample (results not shown here). Such Hertzian behavior of hyperelastic material up to d < 0.3R due to small-strain approximation is also reported by Zhang et al. ⁶⁰ Thus, we will restrict our analysis within d < 0.3R for all cases.

The accuracy of Hertz fitting largely depends on finding the initial point of contact, which is hard to find for extremely compliant surfaces of pAAM hydrogel. In this regards, Garcia et al. developed the dF/du vs F relation (eq 2), derived from the Hertz model, which is free from indentation depth. For our micro- and nanoscale experiments, we use this method. In the first step of the method, a derivative of the force with respect to the arbitrary depth dF/du allows the contact relation to be expressed independently of the depth of contact (Figure 4).

$$F = \frac{4}{3}E^*R^{1/2}d^{3/2} \tag{1}$$

$$\frac{dF}{du} = K_G F^n \tag{2}$$

Here, the true indentation depth = d, the point of first contact = d_0 , and any arbitrary position of the indenter $u = d - d_0$. The derivative used for fitting is a direct function of force F to power n and a coefficient capturing other parameters, K_G (eq 2). Here, $K_G = PK^{1/P}$ and n = (P-1)/P. K is a coefficient containing the constants associated with the force—displacement relationship of a particular

contact model. The coefficient K can represent any power-based contact model. For example, in the Hertzian model, $K=(4/3)E^*R^{0.5}$. The converted power P is the exponent relationship between the force and displacement for the contact model. For instance, Hertzian contact has P=3/2 and n=1/3. The reduced modulus is found from fitting a power-law model to the data by using least-squares error minimization and solving for E^* (and subsequently E) from the coefficient K_G . As a final step, the contact point can be fit on the traditional F-d curve following the fit for E^* . In the case of fitting for E^* as a bulk material property, points at larger depths were only considered, and points at shallow depths only show the deviation from Hertz prediction in the dF/du vs F curve.

3. RESULTS AND DISCUSSION

3.1. Simulation Results. 3.1.1. Case I Results. First, the effect of gradient depth and functional form of the gradient were evaluated. For a linear gradient first described in Figure 2C, the maximum depths of the gradient layer were $d_l = 0.1R$, 0.27R, 0.74R, and 2R. On the force versus depth curve, the shallowest gradient did not deviate from the constant modulus of elasticity E = 20 kPa until the depth was d > 0.8, or d/R > 0.16 (Figure 5A). The intermediate depths show an overall more compliant response, though not reaching the compliance of the reference situation of a Hertz contact with constant modulus of E = 20 kPa. In this view, the greatest differences in the force response appear to the greatest extent for greatest d_l and the compliant surface layer affects the force response even to a depth of 0.2R for gradient layers extending to at least $d_l > 0.1R$

Replotting the indentation curves by using the force differentiated by vertical displacement more appropriately shows the effect of the gradient layer on the overall force response (Figure 5B). All curves are bounded by the Hertz model for samples with homogeneous modulus $E_{\rm s}$ and $E_{\rm b}$, and both these curves have a power of $n=0.\overline{3}$. The curves span in between the two, with the thickest gradient $(d_l=2R)$ resembling the sample of constant low modulus $E_{\rm s}$ for F<10. In addition, each curve shows a power of $n>0.\overline{3}$. With increasing d, the curves approach $n=0.\overline{3}$, though not necessarily reaching the same magnitude of dF/du. The sample with thinner gradient layers approaches $n=0.\overline{3}$ at lower forces.

3.1.2. Case II Results. Laminated samples (case II) showed a similar mechanical response to those with a continuous gradient layer when the number of layers was sufficiently high. As shown in Figures 5C and 5D, all force responses in case II were bounded by the Hertz response with two limiting elastic moduli of E_s and E_b . The control sample for comparison was chosen as the "linear: $d_1 = 2R$ " from case I due to having the same gradient depth d_l . At shallow indentation depths, all samples including the control had a similar force response that overlaps with a Hertz response of stiffness E_s (with shallow defined as $d \le 0.05R$ in Figure 5C and F < 50 in Figure 5D). At this shallow depth, the force response was mainly from the top few layers where there was little difference in elasticity for all cases, which might cause similar response. At progressively larger indentation depths, the underlying layers of different stiffness contributed to the cumulative response. Hence, greatest deviation from Hertzian contact occurred at larger d values. For samples with higher laminated layers $(N \ge 4)$, the local elasticity differed little compared to a sample with a continuous gradient. As a result, the force response of a sample with a large number of laminates emulated the response of a linear gradient layer.

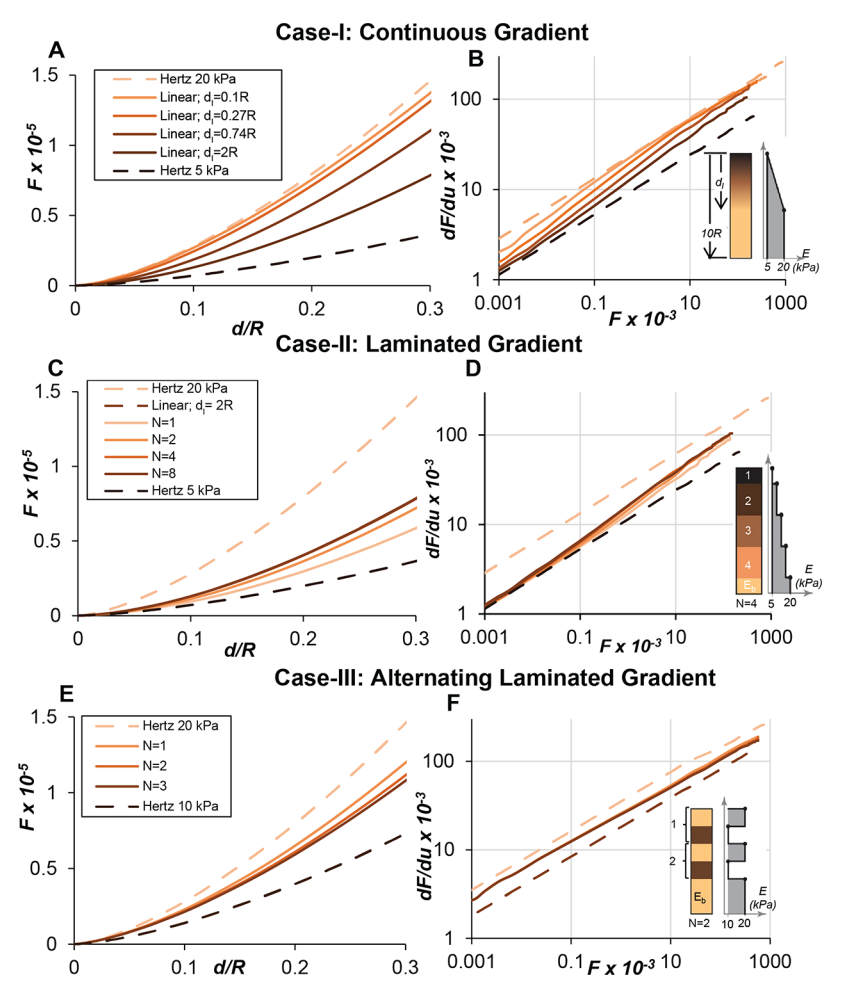


Figure 5. Simulated force response of samples with continuous linear gradient (A, B), laminated gradient (C, D), and alternating laminated gradient (E, F). (A, C, E) Force vs depth curves on a linear scale. (B, D, F) Force derivative with respect to arbitrary indentation depth vs force magnitude. Insets in (B, D, and F) show the schematics and input moduli in each case.

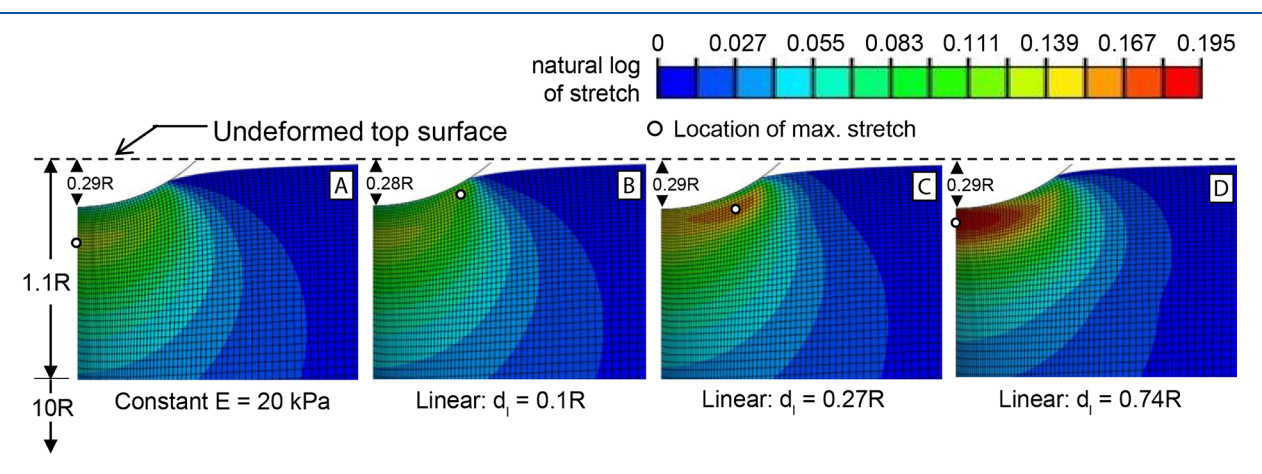


Figure 6. Stretch field contour for linear gradient elasticity samples and the homogeneous sample (A) at an indentation depth, $d \approx 0.29R$. The depth of the gradient layer (d_l) ranges from 0.1R to 0.74R and shown in (B) to (D). The location of the maximum developed stretch is shown as a white bold circle on each of the contour plots. In the case of gradient layers, for d_l smaller than the applied d_r , the stretch field expands both horizontally outward (r-axis) and vertically downward (+z-axis) with increasing d_l (B, C). Once the location reaches to the center with the increase of d_l a further increase in d_l results only in downward vertical expansion of the stretch field (D).

3.1.3. Case III Results. Force responses of alternating laminated layer samples (case III) are shown in Figure 5E,F. All of these samples had a noticeably softer response than a theoretical Hertz response of homogeneous modulus of 20 kPa. At d < 0.15R, the integrated response came mainly from

the top bilayer due to shallow extension of the stretch field into the sample. Thus, samples with identical top bilayer, but different sublayers had identical force responses at shallow depth. With increasing *d*, the stretch field extended further into the depth and caused each alternating bilayer to contribute to

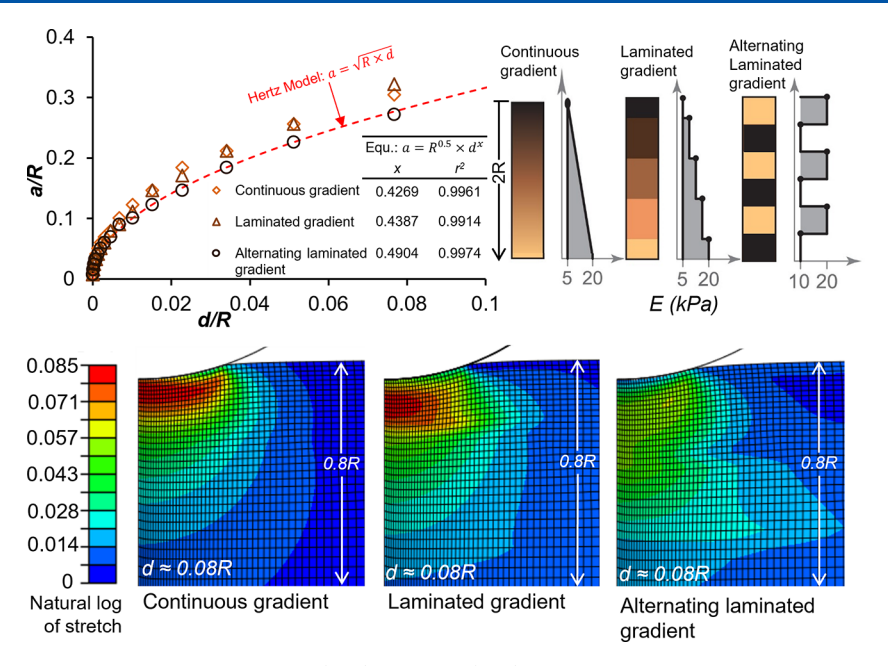


Figure 7. (top) Representative normalized contact radius (a/R) vs depth (d/R) curve for three different samples: continuous gradient (case I), laminated gradient (case II), and alternating laminated gradient (case III). The input modulus E for each case is shown at the top right. (bottom) Contour plots showing the stretch field while indenting at $d \approx 0.08R$. Aside from the alternating laminated case, the samples showed a higher contact radius compared to a Hertzian model. A single parameter power fit was used to establish an empirical relation between a and d and showed in tabular form in the graph.

the overall response, resulting in deviation of the integrated force response. The power fit for all curves resulted in a smaller exponent than the Hertzian exponent $(n = 0.\overline{3})$ due to the softer sublayers. The increasing number of softer sublayers N reduced the exponents n as 0.3212, 0.3137, and 0.3092 for N = 1, 2, and 3, respectively.

3.2. Simulation Discussion. 3.2.1. Stretch Profile in Gradient Layers. The stretch distribution in a gradient layer under a given indentation was found to be significantly different in magnitude and distribution compared to that of a homogeneous sample. For a progressively increasing d on any of the linear gradient samples, the stretch field initially expands into the depth (+z-axis). Once the stretch field has a significant presence in the soft layer, the stiffer bulk restricts further downward propagation of the stretch field. This causes the stretch field to preferentially extend radially along the r-axis. For a fixed indentation depth ($d \simeq 0.29R$), logarithmic stretches for linear gradient samples with different layer thicknesses (d_1) are illustrated in Figure 6 alongside the homogeneous sample. For the homogeneous sample (Figure 6A), the location of maximum stretch (white circle in the contour plot) and the maximum von Mises stress (not shown) were colocated at (r, z) = (0, 0.25R). With increasing d, this location moved vertically downward.

For a continuous gradient sample, unlike the homogeneous one, maximum stress and stretch developed at different locations. With changing d_b the location of the maximum von Mises stress was not strongly affected and developed under the contact in between z = 0.22R and 0.29R. However, for $d_l < d_r$, the location of maximum stretch started near the outer periphery of contact and moved toward the center (r = 0) with increasing d_l (Figure 6B,C). In the case of $d_l \gg d_r$ maximum stretch occurred once again under the indenter (r = 0) and moved vertically into the depth with further increases to d_l (Figure 6D). The location (r, z) of maximum stretch for $d \simeq$

0.29R occurred at (0.46R, 0.05R), (0.381R, 0.11R), and (0, 0.1R) for a gradient layer size of d_l = 0.1R, 0.27R, and 0.74R, respectively. Thus, lateral movement of the stretch field occurred even for thin gradient layers compared to the indentation depth, which likely caused the observed higher contact radius compared to a Hertz prediction. Contact areas larger than models would predict have been experimentally observed in hydrogels with a thin surface layer of gradient cross-link and polymer density. This further supports the notion that the structure and relative stiffness of the surface are major factors in the resulting contact profile and the distribution of stress and stretch in the substrate.

3.2.2. Contact Radius for Gradient Layers. The actual contact radius, a, in simulation was calculated as the radial coordinate of the first node at top surface where the contact pressure dropped to zero for a particular indentation depth, d. For all continuous (case I) and laminated (case II) gradient samples, a was higher than a Hertz prediction (shown in Figure 7). However, a followed the Hertzian relation for all alternating laminated (case II) samples. Three representative samples from three cases were chosen for the sake of discussion. Figure 7 shows a/R versus d/R for three samples. Except for the alternating laminated sample, the simulations showed higher contact radii compared to a Hertzian prediction. Stretch profiles at $d \approx 0.08R$ are shown in the bottom part of Figure 7. For both continuous and laminated samples, a softer top surface causes significant stretch in the radial direction. This results in an increasing deviation from the Hertzian model. In contrast, the top surface of the alternating laminated sample has a stiffer top layer in contact with the indenter. While indenting, maximum stretch occurs within the softer sublayers, which does not significantly affect the contact radius. Thus, a softer top surface on a stiffer substrate surface results in a higher contact radius. A single parameter fitting using $a = R^{0.5} \times d^x$ was performed to establish an empirical

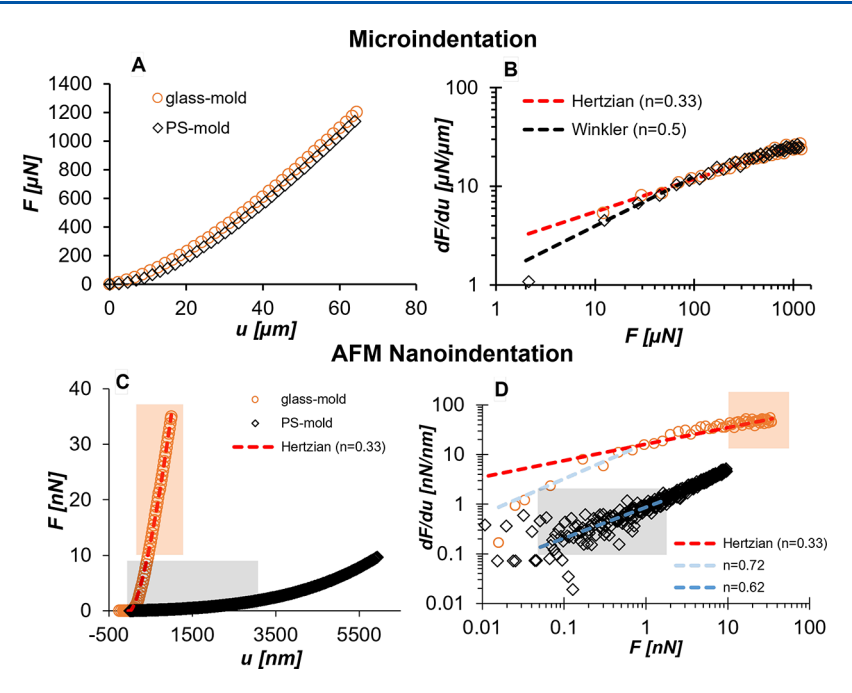


Figure 8. Representative indentation plots of polystyrene (PS) and glass-molded pAAm hydrogels of the same composition at the micro- and nanoscale. Force vs depth data for both samples at microscale (shown in A) and nanoscale (shown in C) indentation. (B) Force derivative with respect to depth vs force, dF vs F, curve for microscale (shown in B) and nanoscale (shown in D) indentation is shown on log-log axes. The red dashed straight lines in (B) and (D) are the single parameter (elastic modulus) fit using eq 2 with a slope of $0.\overline{3}$. For the glass-molded sample, the Hertzian response is observed at the microscale, whereas the non-Hertzian response (light blue dashed line in (D) with n = 0.72) is observed at shallow indentation depth for nanoscale indentation. For the PS-molded sample, the non-Hertzian response is observed at both microscale (black dashed line in (B) with Winkler fitting (n = 0.5)) and nanoscale (dark blue dashed line in (D) with power fitting (n = 0.62)) indentation. Data points within the orange and gray shaded region are used for the Hertzian ($n = 0.\overline{3}$) fit and power fit (n = 0.62), respectively.

relation between a and d. Samples with softer top surface show a lower exponent ($\approx 0.43-0.44$) on d compared to the Hertz exponent (0.5) on d. Johnson and Dunn¹⁷ also reported higher experimentally derived contact radii for the case of a hydrogel with a softer gradient surface using confocal microscopy. Thus, softer top gradient layers in hydrogels stretch more in the radial direction when subjected to indentation, which results in a higher contact radius, a, compared to the Hertz prediction.

3.3. Experimental Results. *3.3.1. Microscale Indentation* Results. Microscale results confirm the simulation results and provide more insight into how the integrated force response changes with scale. Specifically, these larger-scale experiments revealed how the perceived thickness of the gradient layer is sensitive to the scale of the probing technique. As shown in Figure 8A, the force response for both hydrogel samples shows an almost similar response in the F-curve. By use of the Garcia analysis method, indentations of glass-molded and PS-molded hydrogels revealed the noticeable presence of a soft surface layer for the PS-molded hydrogel, but not for the glass-molded hydrogel. The stiffness response at bulk for both the glassmolded and PS-molded hydrogels was similar, with $E_{\text{bulk}} = 27$ kPa (orange dotted line in Figure 8B). The major difference between the hydrogels occurred during the initial tens of micrometers of indentation, where the PS-molded sample experienced non-Hertzian contact behavior spanning a depth of 12 μ m after the Hertz-predicted point of first contact. The glass-molded sample showed non-Hertzian behavior within a probe displacement smaller than the displacement interval of

The initial non-Hertzian contact regime of the indentation into the PS-molded gel is fitted to exponent n (eq 2), showing a larger exponent value of 0.5+ compared to the Hertzian

model exponent value of $n = 0.\overline{3}$. This corresponds to a stronger relationship between the force and displacement P in eq 2 of $F \propto d^2$ or greater. An *n* exponent of 0.5 corresponds to the Winkler foundation model, also termed the "bed of springs" model as it describes the elastic response of a beam or film atop a rigid substrate. Such a structure can result in these samples due to the rigid substrate being the analogy to the stiff bulk, topped by the vanishing density of polymer and crosslinks toward the outer surface. This was shown to imparted by the oxygen content of the contacting mold surface. 15 Previous indentations on these same gels showed n = 0.7 for rigid-probe indentation by Johnson and Dunn.¹⁷ However, this exponent value produces a force-depth relationship of $F \sim d^{3.33}$, which does not correspond to any well-known contact models. The latter portion of both indentation curves fits well to the $n = 0.\overline{3}$ Hertzian model prediction, proving that the response of the bulk polymer is accurately described by Hertzian contact principles.

3.3.2. Nanoscale AFM Indentation Results. AFM nanoindentation reveals the difference in force response due to the thickness variance in gradient layer of chemically equivalent samples. The colloidal probe AFM nanoindentation results for glass- and PS-molded pAAm hydrogels are shown in Figure 8C,D. Force vs depth plots are shown in Figure 8C. The raw data across 20 nm intervals of z-sensor displacement (depth) were averaged to obtain each point in the graph. The glass-molded sample showed a clearly stiffer response compared to the PS-molded sample, which aligns with previous reports from other researchers. The log-log plot of dF vs F in Figure 8D shows that the glass-molded hydrogel had a linear trend at higher force. Points above $F \geq 10$ nN (orange shaded area in Figure 8D) were used to fit for modulus at bulk (E_{bulk}) using

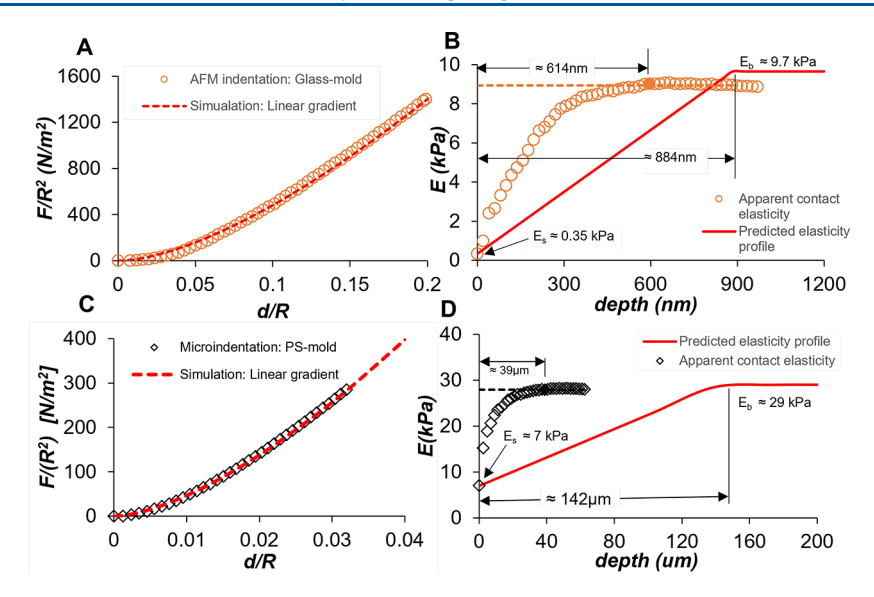


Figure 9. Deconvolution of the material modulus profile using both experimental and simulation data. Normalized Force (F/R^2) vs depth (d/R) curve shows for glass- and PS-molded sample in (A) and (C), respectively. In (B) and (D), points for apparent elasticity are found from an instantaneous Hertzian fit of each point shown in (A) and (C), respectively. Red solid lines in (B) and (D) show the predicted depth-dependent elasticity profile for glass- and PS-molded samples, respectively. The apparent bulk contact modulus (E_{bulk}) is shown here as a dotted line and was found by using the Garcia method.

ı

the Garcia method⁶¹ described in section 2.4. For the glass-molded pAAm hydrogel, we obtained $E_{\text{bulk}} = 11.65 \pm 0.445$ kPa. The mean and the standard deviation were calculated from the experiments at 10 different spots as described in the Materials and Methods section. Gombert et al.²⁶ also reported similar modulus (11 kPa) for the glass-molded pAAm hydrogel with the same composition. The red dashed line in Figure 8C,D shows the Hertz model. At shallow indentation depths in the dF-F plot, the force response for the glass-molded sample deviated from the Hertz response, and the fitted line has a slope of n = 0.72 (light blue dashed line in Figure 8D). In Figure 8D, power fitting was done on all data points less than 3 μ m (0.6R, Hertzian limit for soft material⁴³) depth (gray shaded area in the Figure 8C,D) for the PS-molded sample and found n = 0.62.

The experimental results can be interpreted further within the framework of simulated cases, described in section 3.1.1. For the glass-molded sample, the thickness of the top gradient layer was comparable to R (similar to case I, except with a gradient to 2R). Hence, it showed a gradient response at shallow depths and a Hertzian response at larger indentation depths. For the PS-molded sample, the thickness of the gradient layer was much larger than the indenter radius (5 μ m), which results in this entirely non-Hertzian response. However, the power fit (n) for continuous gradient layer of 2R(case I) in simulation was around 0.36–0.38, depending upon the functional form of gradient, whereas we found n = 0.72 for the PS-molded sample. The possible reasons for this discrepancy were the presence of extremely compliant top layer compared to bulk (in simulation, E_{top} was only 25% of $E_{\rm b}$) in the PS-molded sample. In addition, the depth of the gradient layer was far below that in the simulated cases (discussed in section 2.3.2), which results in a further increase in the power fit exponent.

For a progressive indentation into a sample with softer gradient layer(s), a non-Hertzian response occurred at shallow indentation depths (d), which transformed into a Hertzian response with increasing d. In the F-d and dF-F curves

shown in the Results section, the initial non-Hertzian force response was dominated by the top gradient layers $(n > 0.\overline{3})$ in the dF - F plot). The experimental results at both scales also followed this phenomenon as long as the depth of the gradient layer (d_1) was comparable to the indenter radius (R). With increasing d, the bulk layer significantly contributed to the integrated force response, which followed the Hertzian relation $(n \simeq 0.\overline{3})$. To quantify the minimum indentation depth (d_{Hertz}) required to obtain the Hertz response, we set a quantitative criterion. In the F - d curve, we estimated the apparent contact modulus for each data point by using the Hertz relation. This apparent contact modulus increases with d, starting from E_s , due to the softer top gradient layer. The minimum indentation depth at which this apparent contact modulus reached E_{bulk} was defined as d_{Hertz} . From our simulated results of a continuous linear gradient layer, it could be clearly inferred that d_{Hertz} was smaller than the actual extent of the gradient layer (d_l) . In addition, the contact stiffness E_{bulk} was also smaller than the material modulus of the bulk layer (E_b) . An empirical linear relation between each pair from the simulation results was established and is shown in Figure S4. This information allows layer properties, such as thickness d_l and minimum/maximum moduli E_s/E_b , to be found from contact-derived values of d_{Hertz} and E_{bulk} .

3.4. Experimental Discussion. Our experimental hydrogels with gradient surface layers have an unknown material stiffness profile, which means that the modulus at the top surface (E_s) , modulus in the bulk (E_b) , functional form of the stiffness variation, and extent of the gradient layer (d_i) are not known. In the absence of any suitable model for evaluating the real material's modulus profile, we employ an experiment-to-simulation approach, where the aforementioned simulation-derived relationship between material stiffness and contact stiffness is used to determine the material's modulus profile by using the experimental contact data. We have performed this approach on our experimental data to characterize the gradient layer profile assuming a linear grading, which we refer to as "deconvolution". The simulated force response of a sample

with a deconvoluted material modulus profile is plotted in a normalized F - d curve (see Figure 9A,C) alongside experimental data. Normalizing the data by using eq 3 allows us to compare the force responses across indentations with various R's. The details of the deconvolution process are described in the Supporting Information.

$$\frac{F}{R^2} = \frac{4}{3} \frac{E}{1 - \nu^2} \left(\frac{d}{R}\right)^{1.5} \tag{3}$$

The simulated force response for the predicted gradient profile is plotted as a red dashed line in Figure 9A,C. The simulated force responses for both scales have close agreement with experimental data, which suggests that the linear stiffness model for the hydrogel gradient layer is a suitable approximation of the actual material stiffness profile. As shown in Figure 9B,D, the estimated $d_{\rm Hertz}$ for the glass- and PS-molded samples was 614 nm and 39 μ m, respectively. Gombert et al. ²⁶ also reported a gradient response in the initial 600 nm for a chemically equivalent glass-molded hydrogel. We also estimated the actual depth of the gradient layer as 884 nm and 142 μ m for glass- and PS-molded hydrogels, respectively.

3.5. Contact Pressure in Gradient Surfaces. As discussed above, the softer top gradient layer has two major effects. First, it lowers the force response more than a homogeneous sample with an elasticity of $E_{\rm b}$. Second, it increases the contact area, which cumulatively results in a more significant decrease in contact pressure than the Hertz prediction. To quantify the difference in contact pressure for gradient sample over the Hertz prediction due to gradient layers, we selected continuous linear gradient samples.

As shown in Figure 10, contact pressure developed on a homogeneous sample under indentation closely followed the

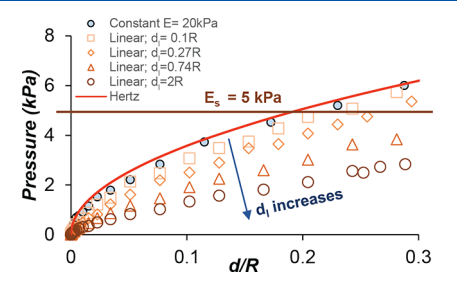


Figure 10. Pressure during indentation for linear gradient samples with different depths of gradient layers (d_l) .

Hertz relation $\left(P \propto \left(\frac{d}{R}\right)^{0.5}\right)$. On the contrary, pressures in linear gradient samples were significantly smaller than the Hertz prediction due to the aforementioned reasons. A simple power fit $\left(P = A\left(\frac{d}{R}\right)^n\right)$ could be useful to estimate the indentation depth dependency on pressure. The exponent (n) of the power fit for all gradient samples (0.63, 0.70, 0.72, and 0.71 for gradient depths of 0.1R, 0.27R, 0.74R, and 2R, respectively) was found significantly higher than the Hertz exponent (0.5). Thus, although the contact pressure develops in a gradient layer sample under indentation is lower in magnitude than homogeneous sample, it has higher sensitivity (i.e., a smaller change in d/R results in a larger change in pressure) on indentation depth.

4. CONCLUSIONS

For the continuous gradient samples in case I, the initial non-Hertzian response $(n > 0.\overline{3})$ is followed by a Hertzian response $(n = 0.\overline{3})$ as the indentation depth increases. The indentation depth at which this transition occurs largely depends on various factors such as the thickness of the gradient layer compared to the indenter radius R, the rate of modulus change over depth in the gradient layer, and the relative compliance of the gradient layer versus the bulk layer. In addition, the actual thickness of the gradient layer was larger than the indentation depth at which the integrated Hertzian response occurred. The actual modulus at the bulk layer is larger than the estimated contact modulus from experiment due to the presence of softer top layers.

Laminated samples in case II can closely mimic the force response of a continuous layer if the layer thicknesses are small compared to indenter radius ($d_l \leq 0.4R$); however, the produced local strain field is significantly different even though their force response is identical. The force response of alternating hard and soft laminates (case III) is largely controlled by the top layer. Looking at the local stretch field for different cases, a softer top layer (in both the continuous and laminated cases) stretches further radially compared to the stiffer bulk layer, which results in a higher contact radius compared to the Hertz prediction. Although the stretch field in alternating laminated layers is different compared to a homogeneous sample, they have similar contact radii as predicted by the Hertz model due to the softer top layer.

The experimental indentation results at both the micro- and nanoscale validate the cohort of simulation results. For microindentation, both the glass- and PS-molded samples showed similar Hertzian responses at higher indentation depths. However, only the PS-molded sample showed a significant non-Hertzian gradient response at indentation depths up to 12 μ m. The glass-molded sample showed a fully uniform Hertzian response at the microscale but experienced both non-Hertzian and Hertzian behavior at the nanoscale. For the PS-molded sample at the nanoscale, only a non-Hertzian response was observed. This phenomena aligns with the previous discussion of the actual gradient layer behavior with respect to the indenter radius R. Our experiment-to-simulation approach is found to be a handy tool to predict the gradient depth with necessary moduli at different layers for glass- and PS-molded samples which is in good agreement with others. 17,26

These results facilitate a better understanding of indentation into gradient samples. This also allows designs of hydrogel samples with gradient layers to obtain a predetermined force response.

ASSOCIATED CONTENT

Supporting Information

The Supporting Information is available free of charge at https://pubs.acs.org/doi/10.1021/acs.langmuir.2c00296.

Additional experimental details in tabular form, schematics of the experimental setup, additional simulation results, and details of the deconvolution process (PDF)

AUTHOR INFORMATION

Corresponding Author

Alison C. Dunn — Department of Mechanical Science and Engineering, University of Illinois Urbana—Champaign, Urbana, Illinois 61801, United States; orcid.org/0000-0002-4841-1293; Phone: +1 (217)300-0349; Email: acd@illinois.edu

Authors

Md Mahmudul Hasan — Department of Mechanical Science and Engineering, University of Illinois Urbana—Champaign, Urbana, Illinois 61801, United States

Christopher L. Johnson – Department of Mechanical Science and Engineering, University of Illinois Urbana–Champaign, Urbana, Illinois 61801, United States

Complete contact information is available at: https://pubs.acs.org/10.1021/acs.langmuir.2c00296

Notes

The authors declare no competing financial interest.

ACKNOWLEDGMENTS

The authors thank the Hutchens group at the University of Illinois Urbana—Champaign for their guidance and server time establishing the simulation methods. This work was supported by NSF Award 1751945. This work was performed in part in the Materials Research Laboratory Central Research Facilities, University of Illinois.

REFERENCES

- (1) Zhang, B.; Han, Q.; Zhang, J.; Han, Z.; Niu, S.; Ren, L. Advanced bio-inspired structural materials: Local properties determine overall performance. *Mater. Today* **2020**, *41*, 177–199.
- (2) Kang, H. W.; Lee, S. J.; Ko, I. K.; Kengla, C.; Yoo, J. J.; Atala, A. A 3D bioprinting system to produce human-scale tissue constructs with structural integrity. *Nat. Biotechnol.* **2016**, *34*, 312–319.
- (3) Tarbell, J. M.; Shi, Z. D. Effect of the glycocalyx layer on transmission of interstitial flow shear stress to embedded cells. *Biomechanics and Modeling in Mechanobiology* **2013**, *12*, 111–121.
- (4) Aoki, S.; Udo, K.; Morimoto, H.; İkeda, S.; Takezawa, T.; Uchihashi, K.; Nishijima-Matsunobu, A.; Noguchi, M.; Sugihara, H.; Toda, S. Adipose tissue behavior is distinctly regulated by neighboring cells and fluid flow stress: A possible role of adipose tissue in peritoneal fibrosis. *Journal of Artificial Organs* **2013**, *16*, 322–331.
- (5) Yue, Y.; Gong, J. P. Structure and unique functions of anisotropic hydrogels comprising uniaxially aligned lamellar bilayers. *Bull. Chem. Soc. Jpn.* **2021**, *94*, 2221–2234.
- (6) Acharya, S.; Gurung, D. B.; Saxena, V. P. Human males and females body thermoregulation: Perfusion effect analysis. *Journal of Thermal Biology* **2014**, *45*, 30–36.
- (7) Fung, Y. C.; Liu, S. Q. Determination of the mechanical properties of the different layers of blood vessels in vivo. *Proc. Natl. Acad. Sci. U. S. A.* **1995**, 92, 2169–2173.
- (8) Cochereau, T.; Bailly, L.; Orgéas, L.; Henrich Bernardoni, N.; Robert, Y.; Terrien, M. Mechanics of human vocal folds layers during finite strains in tension, compression and shear. *J. Biomech.* **2020**, *110*, 109956.
- (9) Nichols, B. A.; Chiappino, M. L.; Dawson, C. R. Demonstration of the mucous layer of the tear film by electron microscopy. *Investigative Ophthalmology and Visual Science* **1985**, 26, 464–473.
- (10) Thissen, H.; Gengenbach, T.; du Toit, R.; Sweeney, D. F.; Kingshott, P.; Griesser, H. J.; Meagher, L. Clinical observations of biofouling on PEO coated silicone hydrogel contact lenses. *Biomaterials* **2010**, *31*, 5510–5519.

- (11) Dunn, A.; Urueña, J.; Huo, Y.; Perry, S.; Angelini, T.; Sawyer, W. Lubricity of Surface Hydrogel Layers. *Tribol. Lett.* **2013**, *49*, 371–378
- (12) Zhang, X.; Xu, J.; Okawa, K.; Katsuyama, Y.; Gong, J.; Osada, Y.; Chen, K. In Situ Monitoring of Hydrogel Polymerization Using Speckle Interferometry. *J. Phys. Chem. B* **1999**, *103*, 2888–2891.
- (13) Kii, A.; Xu, J.; Gong, J. P.; Osada, Y.; Zhang, X. Heterogeneous polymerization of hydrogels on hydrophobic substrate. *J. Phys. Chem. B* **2001**, *105*, 4565–4571.
- (14) Gong, J. P.; Kii, A.; Xu, J.; Hattori, Y.; Osada, Y. A possible mechanism for the substrate effect on hydrogel formation. *J. Phys. Chem. B* **2001**, *105*, 4572–4576.
- (15) Meier, Y. A.; Zhang, K.; Spencer, N. D.; Simič, R. Linking friction and surface properties of hydrogels molded against materials of different surface energies. *Langmuir* **2019**, *35*, 15805–15812.
- (16) Sudre, G.; Hourdet, D.; Cousin, F.; Creton, C.; Tran, Y. Structure of surfaces and interfaces of poly(N,N-dimethylacrylamide) hydrogels. *Langmuir* **2012**, *28*, 12282–12287.
- (17) Johnson, C.; Dunn, A. Tribological characterization of gradient-density polyacrylamide hydrogel surfaces. *Experimental Mechanics* **2021**, *61*, 829–842.
- (18) Simič, R.; Mandal, J.; Zhang, K.; Spencer, N. D. Oxygen inhibition of free-radical polymerization is the dominant mechanism behind the "mold effect" on hydrogels. *Soft Matter* **2021**, *17*, 6394–6403
- (19) Shi, X.; Sharma, V.; Cantu-Crouch, D.; Yao, G.; Fukazawa, K.; Ishihara, K.; Wu, J. Y. Nanoscaled Morphology and Mechanical Properties of a Biomimetic Polymer Surface on a Silicone Hydrogel Contact Lens. *Langmuir* **2021**, *37*, 13961–13967.
- (20) Kontomaris, S.; Malamou, A. Hertz model or Oliver & Pharr analysis? Tutorial regarding AFM nanoindentation experiments on biological samples. *Materials Research Express* **2020**, *7*, 033001.
- (21) Wang, M.; Liu, S.; Xu, Z.; Qu, K.; Li, M.; Chen, X.; Xue, Q.; Genin, G. M.; Lu, T. J.; Xu, F. Characterizing poroelasticity of biological tissues by spherical indentation: An improved theory for large relaxation. *J. Mech. Phys. Solids* **2020**, *138*, 103920.
- (22) Park, S.; Costa, K. D.; Ateshian, G. A. Microscale frictional response of bovine articular cartilage from atomic force microscopy. *J. Biomech.* **2004**, *37*, 1679–1687.
- (23) Rubiano, A.; Galitz, C.; Simmons, C. S. Mechanical Characterization by Mesoscale Indentation: Advantages and Pitfalls for Tissue and Scaffolds. *Tissue Engineering Part C: Methods* **2019**, 25, 619–629.
- (24) Chan, E. P.; Hu, Y.; Johnson, P. M.; Suo, Z.; Stafford, C. M. Spherical indentation testing of poroelastic relaxations in thin hydrogel layers. *Soft Matter* **2012**, *8*, 1492.
- (25) Chandran, P. L.; Dimitriadis, E. K.; Mertz, E. L.; Horkay, F. Microscale mapping of extracellular matrix elasticity of mouse joint cartilage: An approach to extracting bulk elasticity of soft matter with surface roughness. *Soft Matter* **2018**, *14*, 2879–2892.
- (26) Gombert, Y.; Simič, R.; Roncoroni, F.; Dübner, M.; Geue, T.; Spencer, N. D. Structuring hydrogel surfaces for tribology. *Advanced Materials Interfaces* **2019**, *6*, 1901320.
- (27) Pedro, D. I.; Nguyen, D. T.; Trachsel, L.; Rosa, J. G.; Chu, B.; Eikenberry, S.; Sumerlin, B. S.; Sawyer, W. G. Superficial Modulus, Water-Content, and Mesh-Size at Hydrogel Surfaces. *Tribol. Lett.* **2021**, *69*, 1–9.
- (28) Lin, D. C.; Shreiber, D. I.; Dimitriadis, E. K.; Horkay, F. Spherical indentation of soft matter beyond the Hertzian regime: Numerical and experimental validation of hyperelastic models. *Biomechanics and Modeling in Mechanobiology* **2009**, *8*, 345–358.
- (29) Lin, Y.-Y.; Chen, H.-Y. Effect of large deformation and material nonlinearity on the JKR (Johnson–Kendall–Roberts) test of soft elastic materials. *J. Polym. Sci., Part B: Polym. Phys.* **2006**, 44, 2912–2922
- (30) Islam, M. R.; Oyen, M. L. A poroelastic master curve for time-dependent and multiscale mechanics of hydrogels. *J. Mater. Res.* **2021**, *36*, 2582–2590.

- (31) Moghaddam, A. O.; Wei, J.; Kim, J.; Dunn, A. C.; Wagoner Johnson, A. J. An indentation-based approach to determine the elastic constants of soft anisotropic tissues. *Journal of the Mechanical Behavior of Biomedical Materials* **2020**, *103*, 103539.
- (32) Tsukruk, V. V.; Sidorenko, A.; Yang, H. Polymer nanocomposite coatings with non-linear elastic response. *Polymer* **2002**, 43, 1695–1699.
- (33) Bonilla, M. R.; Stokes, J. R.; Gidley, M. J.; Yakubov, G. E. Interpreting atomic force microscopy nanoindentation of hierarchical biological materials using multi-regime analysis. *Soft Matter* **2015**, *11*, 1281–1292.
- (34) Giannakopoulos, A. E.; Suresh, S. Indentation of solids with gradients in elastic properties: Part II. Axisymmetric indentors. *International Journal of Solids and Structures* **1997**, 34, 2393–2428.
- (35) Perriot, A.; Barthel, E. Elastic contact to a coated half-space: Effective elastic modulus and real penetration. *J. Mater. Res.* **2004**, *19*, 600–608
- (36) Constantinescu, A.; Korsunsky, A. M.; Pison, O.; Oueslati, A. Symbolic and numerical solution of the axisymmetric indentation problem for a multilayered elastic coating. *International Journal of Solids and Structures* **2013**, *50*, 2798–2807.
- (37) Zhu, X.; Zhai, J. H.; Xu, W. Analysis of surface-loaded problem of nonhomogeneous elastic half-plane with surface tension. *Mech. Mater.* **2019**, *129*, 254–264.
- (38) Liu, T. J.; Wang, Y. S. Axisymmetric frictionless contact problem of a functionally graded coating with exponentially varying modulus. *Acta Mechanica* **2008**, *199*, 151–165.
- (39) Material parameter identification in functionally graded structures using isoparametric graded finite element model. *Science and Engineering of Composite Materials* **2016**, 23, 685–698.
- (40) Li, Q.; Popov, V. L. Boundary element method for normal non-adhesive and adhesive contacts of power-law graded elastic materials. *Computational Mechanics* **2018**, *61*, 319–329.
- (41) Zelentsov, V. B.; Lapina, P. A.; Mitrin, B. I.; Eremeyev, V. A. Characterization of the functionally graded shear modulus of a half-space. *Mathematics* **2020**, *8*, 1–19.
- (42) Johnson, K. L.; Johnson, K. L. Contact Mechanics; Cambridge University Press: 1987.
- (43) Yoffe, E. Modified Hertz theory for spherical indentation. *Philosophical Magazine A* **1984**, *50*, 813–828.
- (44) Pailler-Mattei, C.; Bec, S.; Zahouani, H. In vivo measurements of the elastic mechanical properties of human skin by indentation tests. *Medical engineering & physics* **2008**, *30*, 599–606.
- (45) Fujimoto, K. L.; Tobita, K.; Merryman, W. D.; Guan, J.; Momoi, N.; Stolz, D. B.; Sacks, M. S.; Keller, B. B.; Wagner, W. R. An elastic, biodegradable cardiac patch induces contractile smooth muscle and improves cardiac remodeling and function in subacute myocardial infarction. *Journal of the American College of Cardiology* 2007, 49, 2292–2300.
- (46) Kuo, C.-H. R.; Xian, J.; Brenton, J. D.; Franze, K.; Sivaniah, E. Complex stiffness gradient substrates for studying mechanotactic cell migration. *Advanced materials* **2012**, 24, 6059–6064.
- (47) Plodinec, M.; Loparic, M.; Monnier, C. A.; Obermann, E. C.; Zanetti-Dallenbach, R.; Oertle, P.; Hyotyla, J. T.; Aebi, U.; Bentires-Alj, M.; Lim, R. Y.; et al. The nanomechanical signature of breast cancer. *Nat. Nanotechnol.* **2012**, *7*, 757–765.
- (48) Shakil, A.; Polycarpou, A. A. High temperature nanomechanical properties of sub-5 nm nitrogen doped diamond-like carbon using nanoindentation and finite element analysis. *J. Appl. Phys.* **2021**, *129*, 135302.
- (49) Zhang, M.-G.; Xu, W.; Wu, T.; Zhang, X.-D.; Zhang, H.; Li, Z.; Zhang, C.; Jiang, H.; Chen, M. Investigation on Mullins effect of rubber materials by spherical indentation method. *Forces in Mechanics* 2021, 4, 100037
- (50) Hassan, A. H. A.; Keleş, İ. FGM Modelling using Dummy Thermal Loads. *Journal of Selcuk International Science and Technology* **2017**, 1..

- (51) Ashirbekob, A.; Abilgaziyev, A.; Kurokawa, S.; Ali, M. H. Modelling of functionally graded materials using thermal loads. *Journal of Engineering Science and Technology* **2020**, *15*, 1719–1730.
- (52) Zhang, K.; Qian, X.; Mei, X.; Liu, Z. An inverse method to determine the mechanical properties of the iris in vivo. *Biomedical engineering online* **2014**, *13*, 1–13.
- (53) Wagner, K.; Cheng, P.; Vezenov, D. Noncontact method for calibration of lateral forces in scanning force microscopy. *Langmuir* **2011**, *27*, 4635–4644.
- (54) Sader, J. E.; Chon, J. W.; Mulvaney, P. Calibration of rectangular atomic force microscope cantilevers. *Review of scientific instruments* **1999**, 70, 3967–3969.
- (55) Sader, J. E.; Borgani, R.; Gibson, C. T.; Haviland, D. B.; Higgins, M. J.; Kilpatrick, J. I.; Lu, J.; Mulvaney, P.; Shearer, C. J.; Slattery, A. D.; et al. A virtual instrument to standardise the calibration of atomic force microscope cantilevers. *Rev. Sci. Instrum.* **2016**, 87, 093711.
- (56) Shoaib, T.; Heintz, J.; Lopez-Berganza, J. A.; Muro-Barrios, R.; Egner, S. A.; Espinosa-Marzal, R. M. Stick—slip friction reveals hydrogel lubrication mechanisms. *Langmuir* **2018**, *34*, 756–765.
- (57) Hertz, H. On Contact Between Elastic Bodies. J. Reine Angew. Math 1882, 94, 156-171.
- (58) Bonyadi, S. Z.; Atten, M.; Dunn, A. C. Self-regenerating compliance and lubrication of polyacrylamide hydrogels. *Soft Matter* **2019**, *15*, 8728–8740.
- (59) Simič, R.; Spencer, N. D. Controlling the friction of gels by regulating interfacial oxygen during polymerization. *Tribol. Lett.* **2021**, 69. 1–10.
- (60) Zhang, M.-G.; Cao, Y.-P.; Li, G.-Y.; Feng, X.-Q. Spherical indentation method for determining the constitutive parameters of hyperelastic soft materials. *Biomechanics and modeling in mechanobiology* **2014**, *13*, 1–11.
- (61) Garcia, M.; Schulze, K. D.; O'Bryan, C. S.; Bhattacharjee, T.; Sawyer, W. G.; Angelini, T. E. Eliminating the surface location from soft matter contact mechanics measurements. *Tribology-Materials, surfaces & interfaces* **2017**, *11*, 187–192.